

# A very-high-energy component deep in the $\gamma$ -ray burst afterglow

<https://doi.org/10.1038/s41586-019-1743-9>

Received: 5 June 2019

Accepted: 30 September 2019

Published online: 20 November 2019

A list of authors and affiliations appears at the end of the paper.

Gamma-ray bursts (GRBs) are brief flashes of  $\gamma$ -rays and are considered to be the most energetic explosive phenomena in the Universe<sup>1</sup>. The emission from GRBs comprises a short (typically tens of seconds) and bright prompt emission, followed by a much longer afterglow phase. During the afterglow phase, the shocked outflow—produced by the interaction between the ejected matter and the circumburst medium—slows down, and a gradual decrease in brightness is observed<sup>2</sup>. GRBs typically emit most of their energy via  $\gamma$ -rays with energies in the kiloelectronvolt-to-megaelectronvolt range, but a few photons with energies of tens of gigaelectronvolts have been detected by space-based instruments<sup>3</sup>. However, the origins of such high-energy (above one gigaelectronvolt) photons and the presence of very-high-energy (more than 100 gigaelectronvolts) emission have remained elusive<sup>4</sup>. Here we report observations of very-high-energy emission in the bright GRB 180720B deep in the GRB afterglow—ten hours after the end of the prompt emission phase, when the X-ray flux had already decayed by four orders of magnitude. Two possible explanations exist for the observed radiation: inverse Compton emission and synchrotron emission of ultrarelativistic electrons. Our observations show that the energy fluxes in the X-ray and  $\gamma$ -ray range and their photon indices remain comparable to each other throughout the afterglow. This discovery places distinct constraints on the GRB environment for both emission mechanisms, with the inverse Compton explanation alleviating the particle energy requirements for the emission observed at late times. The late timing of this detection has consequences for the future observations of GRBs at the highest energies.

On 20 July 2018, GRB 180720B triggered the Fermi Gamma-ray Burst Monitor (GBM) at 14:21:39.65 universal time (UT)<sup>5</sup> ( $T_0$ ) and the Swift Burst Alert Telescope (BAT) 5 s later<sup>6</sup>. Multi-wavelength follow-up observations were performed up to  $T_0 + 3 \times 10^5$  s by the European Southern Observatory's Very Large Telescope, which measured a redshift of  $z = 0.653$  (ref. <sup>7</sup>). In the high-energy  $\gamma$ -ray band (100 MeV–100 GeV) this GRB was also detected by the Fermi Large Area Telescope (LAT) between  $T_0$  and  $T_0 + 700$  s with a maximum photon energy of 5 GeV at  $T_0 + 142.4$  s (ref. <sup>8</sup>). No further high-energy emission was detected in the successive observation windows after 700 s. The prompt emission phase of GRB 180720B is extremely bright, ranking seventh in brightness among the over 2,650 GRBs detected by Fermi-GBM so far (see Methods). With a  $T_{90}$  (the time in which 90% of the flux is detected) of  $48.9 \pm 0.4$  s, GRB 180720B is categorised as a long GRB (typically associated with the death of massive stars<sup>9</sup>), with an isotropic energy release of  $E^{\text{iso}} = (6.0 \pm 0.1) \times 10^{53}$  erg (50–300 keV;  $1 \text{ erg} = 10^{-7} \text{ J}$ ). Observations of this GRB took place using the Swift X-ray Telescope (XRT), identifying a bright afterglow that remained detectable until almost 30 days after  $T_0$  (refs. <sup>10,11</sup>; Fig. 1). In terms of energy flux of the X-ray afterglow (0.3–10 keV, at  $T_0 + 11$  h), this GRB ranks second after the exceptional GRB 130427A<sup>3</sup>.

Observations with the High Energy Stereoscopic System (H.E.S.S.) array began at  $T_0 + 10.1$  h and lasted for two hours. The data were analysed using methods optimized for the detection of the lowest-energy events, revealing a new  $\gamma$ -ray source (Fig. 2a) with an excess of 119  $\gamma$ -ray events and a statistical significance of 5.3 $\sigma$

(5.0 $\sigma$  post-trial; see Methods). The  $\gamma$ -ray excess is well fitted by a point-like source model centred at a right ascension of 00h 02 min 7.6 s and a declination of  $-02^\circ 56' 06''$  (J2000) with a statistical uncertainty of 1.31', consistent with the measurements at other wavelengths<sup>6,8,12</sup>. To rule out the association of this source with an unknown steady  $\gamma$ -ray emitter (such as an active galactic nucleus) or persistent systematic effects, the GRB region was re-observed under similar conditions 18 days after these observations. In total, 6.75 h of data were analysed, resulting in a sky map consistent with background events (Fig. 2b).

The flux spectrum detected by H.E.S.S. (100–440 GeV) was fitted with a function of the form  $F_{\text{obs}}(E) = F_{\text{int}}(E) \times e^{-\tau(E,z)}$ , where the exponential term accounts for the absorption of photons by the extragalactic background light<sup>13</sup>,  $\tau$  is the optical depth and  $F_{\text{int}}(E) = F_{0,\text{int}}(E/E_{0,\text{int}})^{-\gamma_{\text{int}}}$  is a power law describing the intrinsic source emission. The analysis resulted in a photon index of  $\gamma_{\text{int}} = 1.6 \pm 1.2$  (statistical)  $\pm 0.4$  (systematic) and a flux normalization of  $F_{0,\text{int}} = (7.52 \pm 2.03)$  (statistical)  $^{+4.53}_{-3.84}$  (systematic)  $\times 10^{-10} \text{ TeV}^{-1} \text{ cm}^{-2} \text{ s}^{-1}$ , evaluated at an energy of  $E_{0,\text{int}} = 0.154$  TeV (see Methods).

The very-high-energy (VHE) flux, together with measurements at other wavelengths, is shown in Fig. 1. Apart from the exceptionally high flux level, the light curves show a typical power-law behaviour in the X-ray and optical afterglow with a temporal flux decay of the form  $F(t) \propto t^{-\alpha}$  with  $\alpha_{\text{XRT}} = 1.29 \pm 0.01$  and  $\alpha_{\text{optical}} = 1.24 \pm 0.02$ . The spectrum measured by Fermi-LAT (100 MeV–10 GeV) from  $T_0 + 55$  s to  $T_0 + 700$  s is well fitted by a power-law model with photon index  $\gamma_{\text{LAT}} = 2.10 \pm 0.10$ . The light curve in the same time window is fitted by a power law with a temporal decay index of  $\alpha_{\text{LAT}} = 1.83 \pm 0.25$ . It is worth noting that

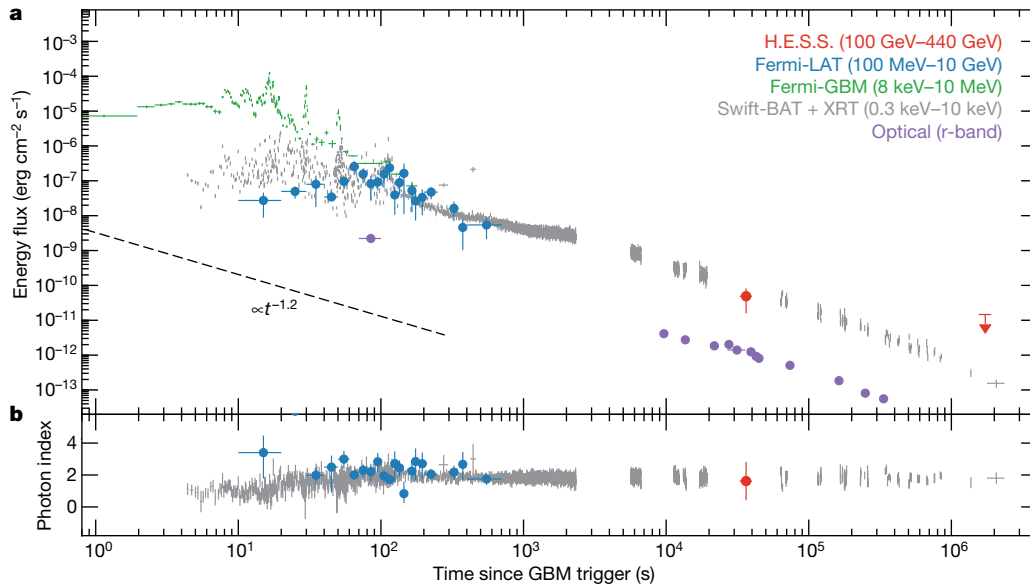


**Fig. 1 | Multi-wavelength light curve of GRB 180720B.** **a**, Energy-flux light curve detected by Fermi-GBM (band fit; green), Fermi-LAT (power law; blue), H.E.S.S. (power-law intrinsic; red) and the optical r-band (purple). The Swift-BAT spectra (15 keV–150 keV) are extrapolated to the XRT band (0.3–10 keV) to produce a combined light curve (grey) and an upper limit (95% confidence

level) for the second H.E.S.S. observation window (power-law intrinsic, red arrow). The black dashed line indicates a temporal decay with  $\alpha = -1.2$ . **b**, Photon index of the Fermi-LAT, Swift and H.E.S.S. spectra. Error bars correspond to  $1\sigma$ .

$\alpha_{\text{LAT}}$  is at about  $1\sigma$  from the mean value of the distribution of the decay indices of long GRBs detected by Fermi-LAT<sup>14</sup> ( $\bar{\alpha}_{\text{LAT}} = 0.99 \pm 0.04$ ,  $\sigma_{\bar{\alpha}} = 0.80 + 0.07$ ) and such deviation could largely depend on the time range in which  $\alpha_{\text{LAT}}$  is fitted, potentially in agreement with  $\alpha_{\text{XRT}}$  and  $\alpha_{\text{optical}}$ .

The detection of VHE  $\gamma$ -ray emission indicates the presence of very energetic particles in the GRB afterglow. This discovery is consistent with efficient  $\gamma$ -ray emission seen in other astrophysical sources with relativistic plasma outflow, for example, pulsar wind nebulae or jets emerging from the nuclei of active galaxies. In the case of a GRB afterglow, the particle acceleration probably occurs at the forward shock<sup>15</sup> (the compression shock wave propagating through the circumburst material), which should be capable of efficient electron and proton acceleration. As proton radiation processes are characterized by long energy-loss timescales relative to the dynamical timescale, the detected  $\gamma$ -ray emission is probably produced by accelerated electrons (see Methods). Therefore, two radiation processes are the most

plausible dominant contributions to the VHE spectrum: synchrotron emission of an electron population in the local magnetic field<sup>16</sup> and synchrotron self-Compton (SSC) scattering<sup>17,18</sup>. In the latter case, the synchrotron photons, which are thought to dominate the target radiation<sup>19</sup>, are inverse-Compton-scattered to higher energies by the same electron population.

The SSC and synchrotron emission origin scenarios<sup>2</sup> place distinctly different demands on the source acceleration efficiency. Whereas an SSC origin requires electrons with only multi-gigaelectronvolt energies, a synchrotron origin requires an extreme accelerator potentially accelerating beyond petaelectronvolt energies<sup>20</sup> (see Methods). Furthermore, for GRBs to operate as  $10^{20}$  eV cosmic-ray sources, they must achieve extreme acceleration<sup>21</sup>. One key distinguishing characteristic between these two emission origins is that SSC predicts the presence of two bumps in the spectral-energy distribution with their height ratio depending on the energy densities of both the electrons and the magnetic field, whereas a synchrotron model implies only a broad

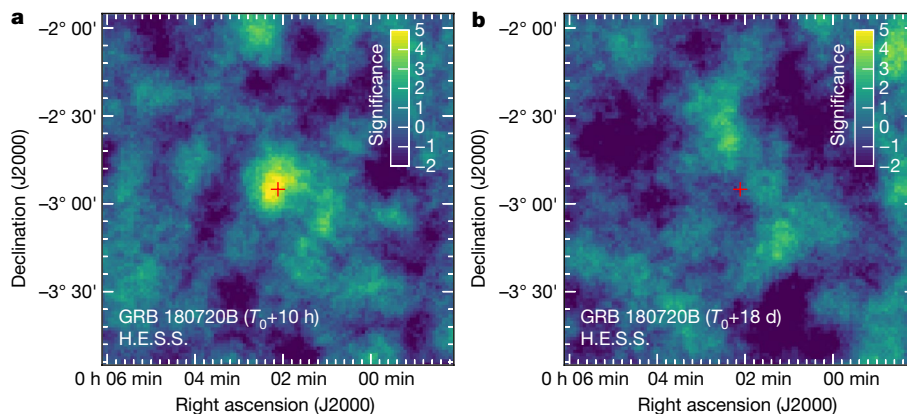


**Fig. 2 | Very-high-energy  $\gamma$ -ray image of GRB 180720B.** Significance map of GRB 180720B field, as observed by H.E.S.S. **a**, Observation made at  $T_0 + 10.1$  h for 2 h. **b**, The same region of the sky, as observed during consecutive nights

between  $T_0 + 18.4$  d and  $T_0 + 24.4$  d. The red cross indicates the position reported by the optical telescope ISON-Castelgrande<sup>12</sup>.

single component. A second difference between these processes is the maximum photon energy achievable.

Considering a synchrotron origin of the broadband afterglow energy spectrum, the highest energy for synchrotron emission from electrons in a maximally efficient accelerator is  $E_{\text{sync}}^{\text{max}} = 9\Gamma mc^2 / (4\alpha_F) \approx 100\Gamma \text{ MeV}$  (with  $\alpha_F$  the fine-structure constant and  $\Gamma$  the bulk Lorentz factor of the forward shock). Thus, for electron synchrotron emission to reach energies beyond 100 GeV 10 h after the prompt emission, a late-time  $\Gamma$  in excess of 1,000 appears to be required. Such a scenario is difficult to realize, with robust expectations suggesting a value of  $\Gamma \approx 20$  at 10 h (see Methods). Alternatively, circumvention of this synchrotron maximum energy limit is possible for scenarios in which either the coherence length of the magnetic turbulence is very small, or different magnetic-field strengths are present in the acceleration and emission zones, or some non-ideal process is responsible for the particle acceleration (see Methods). Regardless of this challenge, this could explain the similarity in the photon index and level of energy flux of the emission seen both at early times by Fermi-LAT and Swift-XRT and at late times by H.E.S.S. and Swift-XRT (Fig. 1). However, the strong requirements for synchrotron emission to extend up to the VHE regime disfavours such origin and the potential onset of a new SSC component should be considered.

The SSC scenario has the advantage that the emission up to VHE at late times is energetically much more easily achievable<sup>23</sup>, leading to the expectation of a new spectral component at VHE. The H.E.S.S. spectral-fit constraints (Extended Data Fig. 1) are consistent with such a possibility within the present uncertainties. Despite this advantage, the potential onset of inverse Compton emission within the Klein–Nishina regime faces challenges (see Methods). Specifically, beyond the  $\gamma$ -ray energy where this sets in, a softer spectral slope and a different brightness evolution of this component<sup>24</sup> are expected. However, interestingly, the presence of synchrotron emission with a hard photon index extending below kiloelectronvolt energies can sufficiently delay the onset of the full Klein–Nishina transition to higher energies (see Methods), beyond that of the VHE detection. The detection of this hard extended synchrotron emission component thus delivers additional supporting evidence for an SSC origin.

This VHE discovery undoubtedly opens a key channel to the understanding of the GRB afterglow phenomena. This measurement proves to be complementary to the VHE-afterglow emission detected in GRB 190829A<sup>25</sup> and the prompt-to-early afterglow emission measured in GRB 190114C by the MAGIC telescopes<sup>26</sup>, providing insight into the nature of GRBs and their VHE detectability. We estimate that future instruments, such as the Cherenkov Telescope Array<sup>27</sup>, will allow up to three more GRB afterglow detections per year in the VHE domain than previously anticipated (see Methods), considerably improving our understanding of GRBs over a diverse range of timescales.

## Online content

Any methods, additional references, Nature Research reporting summaries, source data, extended data, supplementary information, acknowledgements, peer review information; details of author contributions and competing interests; and statements of data and code availability are available at <https://doi.org/10.1038/s41586-019-1743-9>.

- Mészáros, P. Gamma-ray bursts. *Rep. Prog. Phys.* **69**, 2259–2321 (2006).
- Zhang, B. & Mészáros, P. Gamma-ray bursts: progress, problems & prospects. *Int. J. Mod. Phys. A* **19**, 2385–2472 (2004).
- Ackermann, M. et al. Fermi-LAT observations of the gamma-ray burst GRB 130427A. *Science* **343**, 42–47 (2014).
- Piron, F. Gamma-ray bursts at high and very high energies. *C. R. Phys.* **17**, 617–631 (2016).
- Roberts, O. J. et al. GCN22981 – GRB 180720B: Fermi-GBM observation. *GCN Circulars* <https://gcn.gsfc.nasa.gov/gcn3/22981.gcn3> (2018).
- Siegel, M. H. et al. GCN22973 – GRB 180720B: Swift detection of a burst. *GCN Circulars* <https://gcn.gsfc.nasa.gov/gcn3/22973.gcn3> (2018).

- Malesani, D. et al. GCN22996 – VLT/X-shooter redshift. *GCN Circulars* <https://gcn.gsfc.nasa.gov/gcn3/22996.gcn3> (2018).
- Bissaldi, E. et al. GCN22980 – GRB 180720B: Fermi-LAT detection. *GCN Circulars* <https://gcn.gsfc.nasa.gov/gcn3/22980.gcn3> (2018).
- Levan, A. et al. Gamma-ray burst progenitors. *Space Sci. Rev.* **202**, 33–78 (2016).
- Evans, P. A. et al. Methods and results of an automatic analysis of a complete sample of Swift-XRT observations of GRBs. *Mon. Not. R. Astron. Soc.* **397**, 1177–1201 (2009).
- Evans, P. A. et al. An online repository of Swift/XRT light curves of  $\gamma$ -ray bursts. *Astron. Astrophys.* **469**, 379–385 (2007).
- Schmalz, S. et al. GCN23020 – ISON-Castelgrande observation of GRB 180720B. *GCN Circulars* <https://gcn.gsfc.nasa.gov/gcn3/23020.gcn3> (2018).
- Franceschini, A., Rodighiero, G. & Vaccari, M. Extragalactic optical-infrared background radiation, its time evolution and the cosmic photon-photon opacity. *Astron. Astrophys.* **487**, 837–852 (2008).
- Ajello, M. et al. A decade of gamma-ray bursts observed by Fermi-LAT: the second GRB catalog. *Astrophys. J.* **878**, 52 (2019).
- Chevalier, R. A. & Li, Z. Y. Wind interaction models for gamma-ray burst afterglows: the case for two types of progenitors. *Astrophys. J.* **536**, 195–212 (2000).
- Kumar, P. & Barniol Duran, R. On the generation of high-energy photons detected by the Fermi Satellite from gamma-ray bursts. *Mon. Not. R. Astron. Soc.* **400**, L75–L79 (2009).
- Sari, R. & Esin, A. A. On the synchrotron self-Compton emission from relativistic shocks and its implications for gamma-ray burst afterglows. *Astrophys. J.* **548**, 787–799 (2001).
- Zhang, B. & Mészáros, P. High-energy spectral components in gamma-ray burst afterglows. *Astrophys. J.* **559**, 110–122 (2001).
- Warren, D. C. et al. Nonlinear particle acceleration and thermal particles in GRB afterglows. *Astrophys. J.* **835**, 248 (2017).
- Guilbert, P. W., Fabian, A. C. & Rees, M. J. Spectral and variability constraints on compact sources. *Mon. Not. R. Astron. Soc.* **205**, 593–603 (1983).
- Aharonian, F. A., Belyanin, A. A., Derishev, E. V., Kocharovsky, V. V. & Kocharovsky, V. I. V. Constraints on the extremely high-energy cosmic ray accelerators from classical electrodynamics. *Phys. Rev. D* **66**, 023005 (2002).
- Aharonian, F. A. TeV gamma rays from BL Lac objects due to synchrotron radiation of extremely high energy protons. *New Astron.* **5**, 377–395 (2000).
- Warren, D. C., Barkov, M. V., Hirota, I., Nagataki, S. & Laskar, T. Synchrotron self-absorption in GRB afterglows: the effects of a thermal electron population. *Mon. Not. R. Astron. Soc.* **480**, 4060 (2018).
- Nakar, E., Ando, S. & Sari, R. Klein–Nishina effects on optically thin synchrotron and synchrotron self-Compton spectrum. *Astrophys. J.* **703**, 675–691 (2009).
- de Naurois, M. et al. GRB190829A: Detection of VHE gamma-ray emission with HESS. *The Astronomer's Telegram* **13052** (2019).
- Mirzoyan, R. First time detection of a GRB at sub-TeV energies; MAGIC detects the GRB 190114C. *The Astronomer's Telegram* **12390** (2019).
- CTA Consortium. *Science with the Cherenkov Telescope Array* (World Scientific Publishing, 2019).

**Publisher's note** Springer Nature remains neutral with regard to jurisdictional claims in published maps and institutional affiliations.

© The Author(s), under exclusive licence to Springer Nature Limited 2019

**H. Abdalla<sup>1</sup>, R. Adam<sup>2</sup>, F. Aharonian<sup>3,4,5</sup>, F. Ait Benkhali<sup>3</sup>, E. O. Angüner<sup>6</sup>, M. Arakawa<sup>7</sup>, C. Arcaro<sup>1</sup>, C. Armand<sup>8</sup>, H. Ashkar<sup>9</sup>, M. Backes<sup>1,10</sup>, V. Barbosa Martins<sup>11</sup>, M. Barnard<sup>1</sup>, Y. Becherini<sup>12</sup>, D. Berge<sup>11</sup>, K. Bernlöhr<sup>3</sup>, E. Bissaldi<sup>13,14</sup>, R. Blackwell<sup>15</sup>, M. Böttcher<sup>1</sup>, C. Boisson<sup>16</sup>, J. Bolmont<sup>17</sup>, S. Bonnefoy<sup>11</sup>, J. Bregeon<sup>18</sup>, M. Breuhaus<sup>3</sup>, F. Brun<sup>9</sup>, P. Brun<sup>9</sup>, M. Bryan<sup>19</sup>, M. Büchele<sup>20</sup>, T. Bulik<sup>21</sup>, T. Bylund<sup>12</sup>, M. Capasso<sup>22</sup>, S. Caroff<sup>17</sup>, A. Carosi<sup>5</sup>, S. Casanova<sup>3,23</sup>, M. Cerruti<sup>17,24</sup>, T. Chand<sup>1</sup>, S. Chandra<sup>1</sup>, A. Chen<sup>25</sup>, S. Colafrancesco<sup>25,26</sup>, M. Curyto<sup>21</sup>, I. D. Davids<sup>10</sup>, C. Deil<sup>3</sup>, J. Devin<sup>27</sup>, P. deWilt<sup>15</sup>, L. Dirson<sup>26</sup>, A. Djannati-Atai<sup>28</sup>, A. Dmytriiev<sup>16</sup>, A. Donath<sup>3</sup>, V. Doroshenko<sup>22</sup>, J. Dyks<sup>29</sup>, K. Egberts<sup>30</sup>, G. Emery<sup>17</sup>, J.-P. Ernenwein<sup>6</sup>, S. Eschbach<sup>20</sup>, K. Feijen<sup>15</sup>, S. Fegan<sup>2</sup>, A. Fiasson<sup>8</sup>, G. Fontaine<sup>2</sup>, S. Funk<sup>20</sup>, M. Fülling<sup>11</sup>, S. Gabici<sup>28</sup>, Y. A. Gallant<sup>18</sup>, F. Gaté<sup>8</sup>, G. Giavitto<sup>11</sup>, L. Giunti<sup>28</sup>, D. Glawion<sup>31</sup>, J. F. Glicenstein<sup>9</sup>, D. Gottschall<sup>22</sup>, M.-H. Grondin<sup>27</sup>, J. Hahn<sup>3</sup>, M. Haupt<sup>11</sup>, G. Heinzelmann<sup>26</sup>, G. Henri<sup>32</sup>, G. Hermann<sup>3</sup>, J. A. Hinton<sup>3</sup>, W. Hofmann<sup>3</sup>, C. Hoischen<sup>30</sup>, T. L. Holch<sup>33</sup>, M. Holler<sup>34</sup>, D. Horns<sup>26</sup>, D. Huber<sup>34</sup>, H. Iwasaki<sup>7</sup>, M. Jamroz<sup>35</sup>, D. Jankowsky<sup>20</sup>, F. Jankowsky<sup>31</sup>, A. Jardin-Blicq<sup>3</sup>, I. Jung-Richardt<sup>20</sup>, M. A. Kastendieck<sup>26</sup>, K. Katarzyński<sup>36</sup>, M. Katsuragawa<sup>37</sup>, U. Katz<sup>20</sup>, D. Khangulyan<sup>7</sup>, B. Khélifi<sup>28</sup>, J. King<sup>31</sup>, S. Klepser<sup>11</sup>, W. Kluzniak<sup>29</sup>, Nu. Komin<sup>25</sup>, K. Kosack<sup>9</sup>, D. Kostunin<sup>11</sup>, M. Kreter<sup>1</sup>, G. Lamanna<sup>8</sup>, A. Lemièrre<sup>28</sup>, M. Lemoine-Goumard<sup>27</sup>, J.-P. Lenain<sup>17</sup>, E. Leser<sup>11,30</sup>, C. Levy<sup>17</sup>, T. Lohse<sup>33</sup>, I. Lytova<sup>11</sup>, J. Mackey<sup>4</sup>, J. Majumdar<sup>11</sup>, D. Malyshev<sup>22</sup>, V. Marandon<sup>3</sup>, A. Marcowith<sup>18</sup>, A. Mares<sup>27</sup>, C. Mariaud<sup>2</sup>, G. Martí-Devesa<sup>34</sup>, R. Marx<sup>3</sup>, G. Maurin<sup>8</sup>, P. J. Meintjes<sup>38</sup>, A. M. W. Mitchell<sup>3,39</sup>, R. Moderski<sup>29</sup>, M. Mohamed<sup>31</sup>, L. Mohrmann<sup>20</sup>,**

**C. Moore**<sup>40</sup>, **E. Moulin**<sup>9</sup>, **J. Muller**<sup>2</sup>, **T. Murach**<sup>11</sup>, **S. Nakashima**<sup>41</sup>, **M. de Naurois**<sup>2</sup>, **H. Ndiyavala**<sup>1</sup>, **F. Niederwanger**<sup>34</sup>, **J. Niemiec**<sup>23</sup>, **L. Oakes**<sup>33</sup>, **P. O'Brien**<sup>40</sup>, **H. Odaka**<sup>42</sup>, **S. Ohm**<sup>11</sup>, **E. de Ona Wilhelmi**<sup>11</sup>, **M. Ostrowski**<sup>35</sup>, **I. Oya**<sup>11</sup>, **M. Panter**<sup>3</sup>, **R. D. Parsons**<sup>3</sup>, **C. Perennes**<sup>17</sup>, **P.-O. Petrucci**<sup>32</sup>, **B. Peyaud**<sup>19</sup>, **Q. Piel**<sup>8</sup>, **S. Pita**<sup>28</sup>, **V. Poireau**<sup>8</sup>, **A. Priyana Noel**<sup>35</sup>, **D. A. Prokhorov**<sup>25</sup>, **H. Prokoph**<sup>11</sup>, **G. Pühlhofer**<sup>22</sup>, **M. Punch**<sup>12,28</sup>, **A. Quirrenbach**<sup>31</sup>, **S. Raab**<sup>20</sup>, **R. Rauth**<sup>34</sup>, **A. Reimer**<sup>34</sup>, **O. Reimer**<sup>34</sup>, **Q. Remy**<sup>18</sup>, **M. Renaud**<sup>18</sup>, **F. Rieger**<sup>3</sup>, **L. Rinchiuso**<sup>9</sup>, **C. Romoli**<sup>3</sup>, **G. Rowell**<sup>15</sup>, **B. Rudak**<sup>29</sup>, **E. Ruiz-Velasco**<sup>3\*</sup>, **V. Sahakian**<sup>43</sup>, **S. Sailer**<sup>3</sup>, **S. Saito**<sup>7</sup>, **D. A. Sanchez**<sup>8</sup>, **A. Santangelo**<sup>22</sup>, **M. Sasaki**<sup>20</sup>, **R. Schlickeiser**<sup>44</sup>, **F. Schüssler**<sup>9</sup>, **A. Schulz**<sup>11</sup>, **H. M. Schutte**<sup>1</sup>, **U. Schwanke**<sup>33</sup>, **S. Schwemmer**<sup>31</sup>, **M. Seglar-Arroyo**<sup>9</sup>, **M. Senniappan**<sup>12</sup>, **A. S. Seyffert**<sup>1</sup>, **N. Shafi**<sup>25</sup>, **K. Shiningayamwe**<sup>10</sup>, **R. Simoni**<sup>19</sup>, **A. Sinha**<sup>28</sup>, **H. Sol**<sup>16</sup>, **A. Specovius**<sup>20</sup>, **M. Spir-Jacob**<sup>28</sup>, **Ł. Stawarz**<sup>35</sup>, **R. Steenkamp**<sup>10</sup>, **C. Stegmann**<sup>11,30</sup>, **C. Steppa**<sup>30</sup>, **T. Takahashi**<sup>37</sup>, **T. Tavernier**<sup>9</sup>, **A. M. Taylor**<sup>11</sup>, **R. Terrier**<sup>28</sup>, **D. Tiziani**<sup>20</sup>, **M. Tluczykont**<sup>26</sup>, **C. Trichard**<sup>2</sup>, **M. Tsirou**<sup>18</sup>, **N. Tsuji**<sup>7</sup>, **R. Tuffs**<sup>3</sup>, **Y. Uchiyama**<sup>7</sup>, **D. J. van der Walt**<sup>1</sup>, **C. van Eldik**<sup>20</sup>, **C. van Rensburg**<sup>1</sup>, **B. van Soelen**<sup>38</sup>, **G. Vasileiadis**<sup>18</sup>, **J. Veh**<sup>20</sup>, **C. Venter**<sup>1</sup>, **P. Vincent**<sup>17</sup>, **J. Vink**<sup>19</sup>, **H. J. Völk**<sup>3</sup>, **T. Vuillaume**<sup>8</sup>, **Z. Wadiasingh**<sup>1</sup>, **S. J. Wagner**<sup>31</sup>, **R. White**<sup>3</sup>, **A. Wierzcholska**<sup>23,31</sup>, **R. Yang**<sup>3</sup>, **H. Yoneda**<sup>37</sup>, **M. Zacharias**<sup>1</sup>, **R. Zanin**<sup>3</sup>, **A. A. Zdziarski**<sup>29</sup>, **A. Zech**<sup>16</sup>, **A. Ziegler**<sup>20</sup>, **J. Zorn**<sup>3</sup>, **N. Żywucka**<sup>1</sup>, **F. de Palma**<sup>45</sup>, **M. Axelsson**<sup>46,47</sup> & **O. J. Roberts**<sup>48</sup>

<sup>1</sup>Centre for Space Research, North-West University, Potchefstroom, South Africa. <sup>2</sup>Laboratoire Leprince-Ringuet, École Polytechnique, UMR 7638, CNRS/IN2P3, Institut Polytechnique de Paris, Paris, France. <sup>3</sup>Max-Planck-Institut für Kernphysik, Heidelberg, Germany. <sup>4</sup>Dublin Institute for Advanced Studies, Dublin, Ireland. <sup>5</sup>High Energy Astrophysics Laboratory, RAU, Yerevan, Armenia. <sup>6</sup>Aix Marseille Université, CNRS/IN2P3, CPPM, Marseilles, France. <sup>7</sup>Department of Physics, Rikkyo University, Tokyo, Japan. <sup>8</sup>Laboratoire d'Annecy de Physique des Particules, Université Grenoble Alpes, Université Savoie Mont Blanc, CNRS, LAPP, Annecy, France. <sup>9</sup>IRFU, CEA, Université Paris-Saclay, Gif-sur-Yvette, France. <sup>10</sup>Department of Physics, University of Namibia, Windhoek, Namibia. <sup>11</sup>DESY, Zeuthen, Germany. <sup>12</sup>Department of Physics

and Electrical Engineering, Linnaeus University, Växjö, Sweden. <sup>13</sup>Dipartimento Interateneo di Fisica, Politecnico di Bari, Bari, Italy. <sup>14</sup>Istituto Nazionale di Fisica Nucleare, Sezione di Bari, Bari, Italy. <sup>15</sup>School of Physical Sciences, University of Adelaide, Adelaide, South Australia, Australia. <sup>16</sup>LUTH, Observatoire de Paris, PSL Research University, CNRS, Université Paris Diderot, Paris, France. <sup>17</sup>Laboratoire de Physique Nucléaire et de Hautes Energies, LPNHE, Sorbonne Université, Université Paris Diderot, Sorbonne Paris Cité, CNRS/IN2P3, Paris, France. <sup>18</sup>Laboratoire Univers et Particules de Montpellier, Université Montpellier, CNRS/IN2P3, CC 72, Montpellier, France. <sup>19</sup>GRAPPA, Anton Pannekoek Institute for Astronomy, University of Amsterdam, Amsterdam, The Netherlands. <sup>20</sup>Erlangen Centre for Astroparticle Physics, Friedrich-Alexander-Universität Erlangen-Nürnberg, Erlangen, Germany. <sup>21</sup>Astronomical Observatory, The University of Warsaw, Warsaw, Poland. <sup>22</sup>Institut für Astronomie und Astrophysik, Universität Tübingen, Tübingen, Germany. <sup>23</sup>Institut Fizyki Jadrowej PAN, Krakow, Poland. <sup>24</sup>Institut de Ciències del Cosmos (ICC UB), Universitat de Barcelona (IEEC-UB), Barcelona, Spain. <sup>25</sup>School of Physics, University of the Witwatersrand, Johannesburg, South Africa. <sup>26</sup>Institut für Experimentalphysik, Universität Hamburg, Hamburg, Germany. <sup>27</sup>Centre d'Études Nucléaires de Bordeaux Gradignan, Université Bordeaux, CNRS/IN2P3, Gradignan, France. <sup>28</sup>APC, AstroParticule et Cosmologie, Université Paris Diderot, CNRS/IN2P3, CEA/Irfu, Observatoire de Paris, Sorbonne Paris Cité, Paris, France. <sup>29</sup>Nicolaus Copernicus Astronomical Center, Polish Academy of Sciences, Warsaw, Poland. <sup>30</sup>Institut für Physik und Astronomie, Universität Potsdam, Potsdam, Germany. <sup>31</sup>Landessternwarte, Universität Heidelberg, Heidelberg, Germany. <sup>32</sup>Université Grenoble Alpes, CNRS, IPAG, Grenoble, France. <sup>33</sup>Institut für Physik, Humboldt-Universität zu Berlin, Berlin, Germany. <sup>34</sup>Institut für Astro- und Teilchenphysik, Leopold-Franzens-Universität Innsbruck, Innsbruck, Austria. <sup>35</sup>Obserwatorium Astronomiczne, Uniwersytet Jagielloński, Krakow, Poland. <sup>36</sup>Centre for Astronomy, Faculty of Physics, Astronomy and Informatics, Nicolaus Copernicus University, Torun, Poland. <sup>37</sup>Kavli Institute for the Physics and Mathematics of the Universe (WPI), The University of Tokyo Institutes for Advanced Study (UTIAS), The University of Tokyo, Kashiwa, Japan. <sup>38</sup>Department of Physics, University of the Free State, Bloemfontein, South Africa. <sup>39</sup>Physik Institut, Universität Zürich, Zurich, Switzerland. <sup>40</sup>Department of Physics and Astronomy, The University of Leicester, Leicester, UK. <sup>41</sup>RIKEN, Wako, Japan. <sup>42</sup>Department of Physics, The University of Tokyo, Tokyo, Japan. <sup>43</sup>Yerevan Physics Institute, Yerevan, Armenia. <sup>44</sup>Institut für Theoretische Physik, Lehrstuhl IV: Weltraum und Astrophysik, Ruhr-Universität Bochum, Bochum, Germany. <sup>45</sup>Istituto Nazionale di Fisica Nucleare – Sezione di Torino, Turin, Italy. <sup>46</sup>Oskar Klein Centre, Department of Physics, Stockholm University, Stockholm, Sweden. <sup>47</sup>Department of Physics, KTH Royal Institute of Technology, Stockholm, Sweden. <sup>48</sup>Science and Technology Institute, Universities Space Research Association, Huntsville, AL, USA. \*e-mail: contact.hess@hess-experiment.eu

## Methods

### H.E.S.S. and the GRB follow-up programme

The observations presented in this paper were performed using the H.E.S.S. array of imaging atmospheric Cherenkov telescopes, which is situated at an altitude of 1,800 m in the Khomas highlands of Namibia. H.E.S.S. is sensitive to  $\gamma$ -rays in the energy range from tens of gigaelectronvolts to tens of teraelectronvolts. It consists of five Cherenkov telescopes: four with mirror areas of 108 m<sup>2</sup> placed in a square configuration with a side length of 120 m (CT1–CT4) and a single telescope at the centre (CT5) with a mirror area of 614 m<sup>2</sup>. Thanks to its low energy threshold and fast slewing (200° min<sup>-1</sup>)<sup>28</sup>, CT5 is well suited for the observation of soft-spectrum transient sources.

H.E.S.S. maintains an active transient-source observation programme, of which GRBs are an important component. To ensure a fast reaction to GRB alerts, H.E.S.S. is connected to the  $\gamma$ -ray coordinates network (GCN)<sup>29</sup>, which rapidly distributes alerts and observational information from space and ground-based facilities. The target-of-opportunity observation system in H.E.S.S. performs the selection, filtering and processing of these alerts on the basis of source observability and significance, aiming to trigger on bright, precisely located, nearby bursts. Alerts are followed up in two different observation modes. Observations are triggered in the prompt mode when the GRB position is observable from the H.E.S.S. site at the time that the alert is received. In this case, the observation schedule is interrupted and the array is automatically re-pointed to the GRB location. On the other hand, afterglow observations take place for GRBs that become observable only at a later time; such observations are scheduled manually and are triggered by a burst advocate. This was the case for GRB 180720B, which was observed from  $T_0 + 10.1$  h, when the burst position rose above 45° in elevation (below this elevation GRBs are typically not observed owing to the rapid increase in the energy threshold of the H.E.S.S. telescopes). Re-observations were carried out at  $T_0 + 18$  d, after the end of an intervening moonlight period.

### H.E.S.S. data analysis

To reach the lowest possible energies in the analysis presented here, we use only data from the single large telescope (CT5). However, this energy threshold reduction comes at the cost of some angular resolution and sensitivity loss<sup>30</sup>. We present here two hours of observations taken in wobble mode<sup>31</sup>, with the pointing direction of the telescope at an offset of 0.5° from the position provided by Swift-BAT<sup>6</sup>. This observation was made at a mean zenith angle of 31.5° for a total live time of 1.8 h.

To ensure that a potential GRB signal is not diminished by an excessive number of statistical trials, the data analysis is subjected to a strict unblinding procedure. The first step in this unblinding is an inspection of the low-level data, as some calibration artefacts can directly lead to the creation of spurious sources in the field of view. Checks are made on the fractional event participation of each camera pixel (to ensure that single faulty pixels do not dominate the events), the pixel pedestal values and the distribution of events within the field of view. Once these checks are completed, with no artefacts found, the event properties are reconstructed using the ImpACT<sup>32,33</sup> maximum-likelihood-based fitting technique. Background cosmic-ray events are rejected using a neural-network-based scheme<sup>34</sup>. The residual background contamination level of the source region (ON and OFF events) and the ratio of the on-source time to the off-source time ( $\alpha_{\text{Exp}}$ ) are then estimated using the ring method for the production of maps and the reflected-region method when performing the spectral extraction<sup>31</sup>. Full analysis and checks are performed using an additional independent calibration and data analysis chain<sup>35</sup>, serving as a cross-check of all the results.

The source significance is computed using a maximum-likelihood ratio test based on the number of events coming from the source (ON) and the background (OFF) for a given ratio of on-source to off-source

time ( $\alpha$ ; ref. <sup>36</sup>). For the ring method, the number of ON and OFF events is 544 and 4,740, respectively, and  $\alpha_{\text{Exp}} = 0.09$ , resulting in a significance of detection of  $5.3\sigma$ . Similarly the reflected-region method measures 544 ON and 3,998 OFF events and  $\alpha_{\text{Exp}} = 0.11$  at a significance of  $4.6\sigma$ , which is verified by the cross-check analysis, which provided 651 ON and 5,200 OFF events and  $\alpha_{\text{Exp}} = 0.10$  with a significance of  $4.5\sigma$ .

The source morphology is fitted with a two-dimensional likelihood procedure by assuming point-like and Gaussian source models convolved with the expected energy-dependent point spread function (obtained from simulations) and the measured source spectrum. Both source models are proved to be compatible with the morphology of the discovered source, with no statistically significant preference for source extension shown.

Spectral analysis is performed using the forward-folding method<sup>37</sup>, which corrects for the limited energy resolution of the single-telescope event reconstruction. The measured source spectrum is obtained by fitting a simple power-law model of the form  $F_{\text{obs}}(E) = F_{0,\text{obs}}(E/E_{0,\text{obs}})^{\gamma_{\text{obs}}}$ , where  $F_{0,\text{obs}}$  is the flux normalization,  $\gamma_{\text{obs}}$  is the photon index and  $E_{0,\text{obs}}$  is the reference energy. However, owing to the absorption of the most energetic photons by the extragalactic background light (EBL), the apparent photon index of this source will be somewhat steeper than the intrinsic photon index. The intrinsic spectrum  $F_{\text{int}}(E)$  is therefore obtained by fitting the measured spectrum with an attenuated power-law model,  $F_{\text{obs}}(E) = F_{\text{int}}(E) \times e^{-\tau(E,z)} = F_{0,\text{int}}(E/E_{0,\text{int}})^{\gamma_{\text{int}}} \times e^{-\tau(E,z)}$ , where the last term in the equation corresponds to the EBL absorption coefficient predicted<sup>13</sup> for a redshift of 0.653. The best-fit spectra, together with the spectral points, are shown in Extended Data Fig. 1, and the spectral parameters are summarized in Extended Data Table 1.

Systematic uncertainties in the fitted spectra are determined by accounting for a 15% uncertainty in the reconstructed energy due to possible variations in the measured Cherenkov light yield<sup>38</sup>. The measured energy is systematically shifted by  $\pm 15\%$  and the whole spectral-fitting procedure is redone. In addition, short dips in the trigger rate (at the level of 30%) were identified in the data, which can probably be attributed to the presence of high-altitude clouds. To assess the effect of these, the time windows containing such trigger rate features (21.7 min total) were removed from the data and the standard analysis described above was performed on the reduced dataset. From this, we conclude an additional systematic underestimation of 32% and 4.8% in the measured normalization and photon index, respectively. These two sources of systematic uncertainty are considered to be independent and are therefore added in quadrature for the estimation of the total systematic uncertainty.

The intrinsic spectrum was obtained with a chosen EBL model<sup>13</sup>. To determine how this choice influences the results presented in this work, the data were re-analysed using three additional EBL models<sup>39–41</sup>, each one employing a different approach to predict the overall EBL level<sup>39</sup>. The absorption coefficient for a redshift of 0.653 within the energy range of the detected emission does not present sizeable deviations between the models considered (Extended Data Fig. 2). When employing these EBL models for the spectral fit, a change of up to 55.3% and 27% was found in the reported normalization and index, respectively. The statistical uncertainty on the fitted spectra remains the biggest source of uncertainty in the results.

### Trial correction

Since 2012, H.E.S.S. has performed five additional follow-up observations of well localized GRBs (Swift and Fermi-LAT alerts) using only CT5 (similar to the observations presented here). The significance distribution of this sample (excluding GRB 180720B) is consistent with pure statistical fluctuations. Therefore, the post-trial significance for GRB 180720B can be assessed by accounting for these previously observed GRBs. This results in a post-trial significance of  $4.3\sigma$  (reflected-region method) and  $5.0\sigma$  (ring method). As the analysis of GRB 180720B was

performed once under the aforementioned unblinding procedure, no additional trials have been added to the results presented here.

### Background systematic effects

Systematic effects on the sky map background (Fig. 2) were determined by measuring the significance distribution when excluding the source region. Although a normal distribution was expected, a width of 1.09 was measured in this significance distribution, therefore adding a slight shift to the reported significance of the ring method (used in the production of sky maps). The corrected significance when accounting for such effects is  $4.9\sigma$  ( $4.7\sigma$  post-trial). Nonetheless, this measured distribution depends strongly on the parameters of the ring method and should be subject to statistical uncertainties.

### Fermi data analysis

The Fermi-GBM data for GRBs are publicly available through the GBM Burst Catalog at HEASARC<sup>42</sup>. For GRB 180720B the available time-tagged events of those detectors having the best viewing angle to the Swift-XRT position—namely, n6, n7, nb and b1—were analysed. Temporally resolved energy-flux data points (Fig. 1) were obtained with the RMfit analysis software<sup>43</sup> by combining time-tagged event data from all four detectors into 256-ms bins in the energy range from 8 keV to 10 MeV.

The analysis of the Fermi-LAT data was performed using the ‘Pass8’<sup>44</sup> processed events. We used the P8R3\_TRANSIENTO10E event class, which is suitable for transient-source analysis, and the corresponding instrument response functions<sup>45</sup>. Events were selected from  $T_0$  to  $T_0 + 700$  s in the standard GRB analysis energy range of 100 MeV–100 GeV over a region of  $10^\circ$  around the Swift-XRT localization. Event selection, quality cuts and data analysis were performed with the standard FermiTools<sup>46</sup> software. The source detection over the full duration was determined by a likelihood analysis providing a test-statistic value of  $TS \approx 600$ , which corresponds to a significance of  $\sigma \approx 25$  ( $\sigma \approx \sqrt{TS}$ ).

Because the highest-energy photon detected has an energy of 5 GeV (at  $T_0 + 142.4$  s), the temporally resolved energy-flux data points (Fig. 1) were computed in the energy range from 100 MeV to 10 GeV. The analysis model included the Galactic interstellar emission model (gll\_iem\_v06.fits) and the relative isotropic-diffuse-emission templates provided by the Fermi-LAT collaboration<sup>47</sup>, and the normalization of the latter was left free to vary. The spectrum for each bin was fitted by a single power-law model  $F(E) = F_0 \times (E/E_0)^{-\gamma}$ , with the flux normalization  $F_0$  and the photon index  $\gamma$  as free parameters. As no emission with energies  $>10$  GeV was detected, no additional term was required to account for EBL absorption<sup>13</sup> in the spectra. The temporal decay  $\alpha_{\text{LAT}}$  was fitted by a power-law model using a least-squares technique applied from  $T_0 + 55$  s to  $T_0 + 700$  s in order to ensure no contamination of the prompt emission observed by Fermi-GBM and Swift-BAT, obtaining a reduced  $\chi^2$  of  $\chi^2 = 0.63$  (14 degrees of freedom).

### Optical data

The optical data shown in Fig. 1 were compiled from the GCN circulars of observations performed in the r-band by the following instruments: Kanata<sup>48</sup>, MITSuME<sup>49</sup>, TSHAO<sup>50</sup>, MASTER-K<sup>51</sup>, MASTER-I, ISON-Castelgrande<sup>12</sup>, OSN<sup>52</sup>, LCO<sup>53</sup> and KAIT<sup>54</sup>. The reported temporal decay index  $\alpha_{\text{optical}}$  was measured from  $T_0 + 9,642$  s to  $T_0 + 3.35 \times 10^5$  s by performing a power-law fit with a  $\chi^2$  fitting procedure.

### Swift data

The Swift data are publicly available through the Swift online repository<sup>55</sup>. The temporally resolved energy-flux data shown in Fig. 1 were obtained using the Burst Analyser tool<sup>10,11</sup>. The data were rebinned to give a signal-to-noise ratio of 7 and systematic uncertainties were included. The temporal decay reported here ( $\alpha_{\text{XRT}}$ ) was obtained from  $T_0 + 2,200$  s to  $T_0 + 3.05 \times 10^5$  s and corresponds to the fourth break in the light curve, as identified from the fitting procedures of the Swift-XRT tools.

### Cherenkov Telescope Array detectability prospects

Considering the Cherenkov Telescope Array (CTA) to be an order of magnitude more sensitive than the H.E.S.S. array implies that it will have the ability to detect energy fluxes  $\sim 10$  times fainter than that of GRB 180720B at VHE. If the VHE flux equals that detected by Swift-XRT, as suggested by our measurements (Fig. 1), we estimate the occurrence of three GRBs per year above this flux, which will therefore be detectable by CTA (Extended Data Fig. 3). This number could be increased for follow-up observations at earlier times. By assuming a temporal decay value of  $\alpha = 1.2$  ( $F(t) \propto t^{-\alpha}$ ) for all the GRB afterglows detected by Swift-XRT<sup>56</sup>, an extrapolation of the 11-h energy flux to that expected at 5 h provides a detectability prospect of  $\sim 10$  GRBs per year at such follow-up delay times. It should be noted, however, that the presence of VHE emission could also be dependent on the GRB environment<sup>57</sup>, and this influence was not considered in this estimation.

### Bulk Lorentz factor

The bulk Lorentz factor depends on two factors: the released energy and the density of the circumburst medium<sup>58</sup>,  $\Gamma = \sqrt{E^{\text{iso}}/(Mc^2)}$ , where  $E^{\text{iso}}$  is the equivalent isotropic energy and  $M$  is the total mass swept up by the shock. The latter depends on the nature of the circumburst environment:  $M = (4\pi/3)R^3 n m_p$  for a homogeneous medium (here  $n$  is the medium number density,  $R$  is the shock radius and  $m_p$  is the proton mass) and  $M = \dot{M}_* R / v_*$  for a shock propagating in a constant-velocity wind (here  $\dot{M}_*$  and  $v_*$  are the wind mass-loss rate and velocity, respectively). The shock radius depends on the detection time as  $R \approx A_R F^2 t c / (1+z)$ , where  $A_R = 8$  for a homogeneous medium and  $A_R = 4$  for wind environments ( $c$ , speed of light in vacuum). Thus, for GRB 180720B ( $t = 10$  h,  $z = 0.653$ , and  $E^{\text{iso}} \approx 10^{54}$  erg) one obtains  $\Gamma = 15 n_0^{-1/8}$  (here  $n_0 = n / (1 \text{ cm}^{-3})$ ) for a homogeneous medium or  $\Gamma = 20 \dot{M}_{*, -5}^{-1/4} v_{*, 3.3}^{1/4}$  (here  $\dot{M}_{*, -5} = \dot{M}_* / (10^{-5} M_\odot \text{ yr}^{-1})$  and  $v_{*, 3.3} = v_* / (2,000 \text{ km s}^{-1})$ ) for a wind environment.

### Non-thermal process efficiency

The non-thermal process efficiency,  $\kappa = t_{\text{dyn}}/t_{\text{cool}}$ , depends on the ratio of the shock dynamic timescale,  $t_{\text{dyn}} = R/(c\Gamma)$ , to the cooling time,  $t_{\text{cool}}$ , which depends on the radiation mechanism, the density of the target and the energy of the parent particles. For hadronic processes<sup>59</sup>, which include proton–proton ( $pp$ ) and photon–meson ( $p\gamma$ ) channels, the radiation efficiency is  $\kappa_{pp} \approx 10^{-7} [R/(10^{18} \text{ cm})] n_0$  and  $\kappa_{p\gamma} \approx 3 \times 10^{-4} (I/20)^2 [R/(10^{18} \text{ cm})] (\kappa/10^{-2}) [E_i/(1 \text{ keV})]^{-1} n_0$  (here  $\kappa$  is the total radiative efficiency and  $E_i$  is the peak frequency of the soft-emission component). These low efficiencies favour the electromagnetic processes<sup>60</sup>. The efficiency of the synchrotron channel for the emission detected in the VHE band,  $E \approx 100$  GeV, is  $\kappa_{\text{sync}} = 5 \times 10^7 (m_e/m)^{5/2} [R/(10^{18} \text{ cm})] (\eta_B/0.1)^{3/4} \eta_{\text{turb}}^{-1/2} n_0^{3/4}$ , where  $m_e$  and  $m$  are the masses of the electron and the emitting particle, respectively,  $\eta_B$  is a fraction of the internal energy contained in the magnetic field and  $\eta_{\text{turb}} = \max(1, R_{\text{Lar}}^{\text{nr}}/\lambda_{\text{cor}})$  defines the shift of the peak energy if a charged particle interacts with a turbulent magnetic field<sup>61</sup> (here  $R_{\text{Lar}}^{\text{nr}}$  is the non-relativistic Larmor radius and  $\lambda_{\text{cor}}$  is the magnetic-field correlation length). If the inverse Compton scattering proceeds in the Thomson regime, then  $\kappa_{\text{IC}} = 3(I/20) [\kappa/(10^{-2})] [R/(10^{18} \text{ cm})] [E_i/(1 \text{ keV})]^{-1/2} n_0$ . Efficiencies larger than 1 indicate that particle cooling occurs faster than the source dynamical timescale and is therefore highly efficient.

### Synchrotron emission

Synchrotron emission is characterized by the highest radiation efficiency, but this emission component peaks below the limiting energy of  $E_{\text{sync}}^{\text{max}} = 100 \Gamma (m/m_e) \eta_{\text{turb}} (B_{\text{em}}/B_{\text{ac}}) (E_{\text{ac}}/B_{\text{ac}})$  MeV. Here  $B_{\text{em}}$  and  $B_{\text{ac}}$  are the magnetic-field strengths at the emitter and accelerator sites, respectively. The accelerating electric field,  $E_{\text{ac}}$ , is smaller than the magnetic field,  $E_{\text{ac}} < B_{\text{ac}}$ , if the particle acceleration proceeds in ideal magnetohydrodynamic flows<sup>21</sup>. Thus, the production of VHE  $\gamma$ -rays via electron synchrotron emission requires a large Lorentz factor,  $\Gamma > 10^3$ , a very-small-scale magnetic turbulence,  $\lambda_{\text{cor}} < 10^{-2} R_{\text{Lar}}^{\text{nr}}$ , a large change

# Article

of the magnetic-field strength,  $B_{\text{em}} > 10^2 B_{\text{ac}}$ , particle acceleration to operate in the non-ideal magnetohydrodynamic regime, or a combination of these factors. Proton synchrotron emission alleviates these requirements, but at the expense of a significantly lower radiation efficiency. Whereas proton synchrotron emission dominates over other hadronic radiation processes in terms of efficiency<sup>18</sup>, its efficiency is still considerably smaller than that of electrons. Thus proton synchrotron emission is expected to give rise only to a subdominant emission component within the VHE band.

## Energy of particles emitting in the VHE regime

The energy of particles emitting in the VHE regime depends on the dominant radiation mechanism and the properties of the ejecta. In the case of a synchrotron origin scenario, the particle energy is determined by three important factors: the shock Lorentz factor, the strength of the magnetic field and the turbulence scale. The first factor,  $\Gamma \approx 20$ , is relatively well defined by the epoch of the H.E.S.S. observation, but the magnetic-field strength and the possibility of small-scale turbulence remain highly uncertain. The internal energy density,  $\sim 0.1(\Gamma/20)^2 n_0 \text{J m}^{-3}$ , suggests that a Gauss-strength magnetic field is expected for the case of energy equipartition between the magnetic field and particles. We note, however, that substantially smaller plasma magnetization is reported in the literature<sup>62</sup>, corresponding to weaker magnetic fields by several orders of magnitude. Assuming that synchrotron emission beyond the 100 MeV energy limit in the co-moving frame can be achieved, the energy of the emitting electrons can be estimated as  $E_e \approx 4[E/(100 \text{ keV})]^{1/2}(\Gamma/20)^{-1/2}[B/(0.1 \text{ G})]^{-1/2}n_{\text{turb}}^{-1/2} \text{TeV}$ . The production of 100-GeV  $\gamma$ -rays through a synchrotron scenario therefore requires electrons of ultrahigh-energy,  $E_e \approx 4 \text{ PeV}$ , unless a configuration with a very-small-scale turbulence is present. The energy of particles that provide the dominant contribution to the inverse Compton emission depends strongly on the spectrum of the target photons and the bulk Lorentz factor. An electron with energy  $E_e$  up-scatters a target photon with energy  $E_t$  to an energy of  $\min\{E_e[E_e/(m_e c^2)]^2, \Gamma E_t\}$ . For target photons detected in the X-ray energy band,  $E_t \approx 1 \text{ keV}$ , electrons with energy of  $E_e \approx 10 \text{ GeV}$ , which in the laboratory frame have an energy of hundreds of gigaelectronvolts, can produce  $\gamma$ -rays that are detected in the VHE band.

## Target photons

Target photons of very different energies can be up-scattered to  $\gamma$ -rays of the same energy. This can be of particular relevance for VHE  $\gamma$ -rays detected from GRBs, where both the target photons and non-thermal electrons probably have broad energy distributions. Assuming a power-law distribution for the target photon flux,  $dn/dE_t \propto E_t^{-\gamma}$ , and for electrons,  $dn_e/dE_e \propto E_e^{-\gamma_e}$ , one finds that the relative contribution to the  $\gamma$ -ray emission depends on the electron energy as  $\propto \{1 - [E/(E_e \Gamma)]\} E_e^{2\gamma - \gamma_e}$ . For simplicity, just a single high-energy term in the cross-section was accounted for (resulting in the factor  $1 - [E/(E_e \Gamma)]$ ), which is sufficient for a qualitative study. However, the obtained dependence shows that for a reasonable range of photon and electron indices,  $1.5 < \gamma, \gamma_e < 3$ , the highest-available-energy electrons may provide an important contribution to the  $\gamma$ -ray energy band by up-scattering photons with energies within the infrared-to-ultraviolet range.

## Klein–Nishina cutoff

The Klein–Nishina cutoff is a substantial reduction of the Compton cross-section that occurs when  $E_e E_t \gtrsim \Gamma m_e^2 c^4$ , where  $E_e$  and  $E_t$  are the electron and target photon energies in the co-moving frame and the laboratory system, respectively. This results in a softening of the  $\gamma$ -ray spectrum that occurs for  $E \gtrsim 50(\Gamma/20)^2 [E_t/(1 \text{ keV})]^{-1} \text{GeV}$ . Because typically the GRB synchrotron spectral-energy distribution peaks in the kiloelectronvolt band, the inverse Compton component detected at late afterglow phases may be affected by the Klein–Nishina cutoff, resulting in reduced fluxes and steeper spectra. This may appear to

contradict the relatively hard intrinsic spectral index of  $\gamma_{\text{int}} \approx 1.6$  inferred from the H.E.S.S. measurement. There are, however, two effects that can result in spectral hardening at energies around the cutoff: (i) the up-scattering of low-energy infrared-to-ultraviolet photons, which give an intrinsic VHE component with the same slope as that seen in the hard-X-ray band and (ii) the hardness of the electron spectrum at gigaelectronvolt energies, where adiabatic losses probably render the electron spectrum hard. The search for consistency within this framework of the hard VHE spectrum with the SSC scenario, however, requires detailed dedicated simulations, which are beyond the scope of this observational paper.

## Data and code availability

The raw H.E.S.S. data and the code used in this study are not public, but belong to the H.E.S.S. collaboration. All derived higher-level data that are shown in the plots will be made available on the H.E.S.S. collaboration's website upon publication of this study. Data and analysis code from the Fermi-GBM and LAT instruments are publicly available. Links to the data and software are provided in the Methods section. This work also made use of data supplied by the UK Swift Science Data Centre at the University of Leicester (<http://www.swift.ac.uk/archive/>).

- Hofverberg, P. et al. Commissioning and initial performance of the H.E.S.S. II drive system. In *Proc. of the 33rd International Cosmic Ray Conference (ICRC 2013)*, 3092 (Curran Associates, 2013).
- Bathelmy, S. GCN: The gamma-ray burst coordinates network <http://gcn.gsfc.nasa.gov> (2019).
- Holler, M. et al. Observations of the Crab Nebula with H.E.S.S. Phase II. *PoS Proc. Sci. ICRC2015*, **847** (2016).
- Berge, D., Funk, S. & Hinton, J. Background modelling in very-high-energy gamma-ray astronomy. *Astron. Astrophys.* **466**, 1219–1229 (2007).
- Parsons, R. D. & Hinton, J. A. A Monte Carlo template based analysis for air-Cherenkov arrays. *Astropart. Phys.* **56**, 26–34 (2014).
- Parsons, R. D., Murach, T. & Gajdus, M. HESS II data analysis with ImpACT. *PoS Proc. Sci. ICRC2015*, **826** (2015).
- Murach, T., Gajdus, M. & Parsons, R. D. A neural network-based monoscopic reconstruction algorithm for H.E.S.S. II. *PoS Proc. Sci. ICRC2015*, **1022** (2015).
- de Naurois, M. & Rolland, L. A high performance likelihood reconstruction of  $\gamma$ -rays for imaging atmospheric Cherenkov telescopes. *Astropart. Phys.* **32**, 231–252 (2009).
- Li, T. P. & Ma, Y. Q. Analysis methods for results in gamma-ray astronomy. *Astrophys. J.* **272**, 317–324 (1983).
- Piron, F. et al. Temporal and spectral gamma-ray properties of Mkn 421 above 250 GeV from CAT observations between 1996 and 2000. *Astron. Astrophys.* **374**, 895–906 (2001).
- Abdalla, H. et al. Gamma-ray blazar spectra with H.E.S.S. II mono analysis: the case of PKS 2155-304 and PG 1553+113. *Astron. Astrophys.* **600**, A89 (2017).
- Domínguez, A. et al. Extragalactic background light inferred from AEGIS galaxy-SED-type fractions. *Mon. Not. R. Astron. Soc.* **410**, 2556–2578 (2011).
- Finke, J. D., Razzaque, S. & Dermer, C. D. Modeling the extragalactic background light from stars and dust. *Astrophys. J.* **712**, 238–249 (2010).
- Gilmore, R. C. et al. Semi-analytic modelling of the extragalactic background light and consequences for extragalactic gamma-ray spectra. *Mon. Not. R. Astron. Soc.* **422**, 3189–3207 (2012).
- FERMIGBRST – Fermi GBM Burst Catalog <https://heasarc.gsfc.nasa.gov/W3Browse/fermi/fermigbrst.html> (2019).
- GBM Software Tools <https://fermi.gsfc.nasa.gov/ssc/data/analysis/rmfrit/> (2019).
- Atwood, W. et al. Pass 8: toward the full realization of the Fermi-LAT scientific potential. In *2012 Fermi Symposium proceedings, eConf C121028* (2013); preprint at <https://arxiv.org/abs/1303.3514>.
- Fermi LAT Performance [http://www.slac.stanford.edu/exp/glast/groups/canda/lat\\_Performance.htm](http://www.slac.stanford.edu/exp/glast/groups/canda/lat_Performance.htm) (2019).
- Fermitools-conda-recipe <https://github.com/fermi-lat/Fermitools-conda/> (2019).
- Acero, F. et al. Development of the model of galactic interstellar emission for standard point-source analysis of Fermi Large Area Telescope data. *Astrophys. J. Suppl. Ser.* **223**, 26 (2016).
- Sasada, M. et al. GCN22977 – Kanata observation. *GCN Circulars* <https://gcn.gsfc.nasa.gov/gcn3/22977.gcn3> (2018).
- Itoh, R. et al. GCN22983 – MITSuME Akeno observation. *GCN Circulars* <https://gcn.gsfc.nasa.gov/gcn3/22983.gcn3> (2018).
- Reva, I. et al. GCN22979 – TSHAO observation. *GCN Circulars* <https://gcn.gsfc.nasa.gov/gcn3/22979.gcn3> (2018).
- Lipunov, V. et al. GCN23023 – MASTER observation. *GCN Circulars* <https://gcn.gsfc.nasa.gov/gcn3/23023.gcn3> (2018).
- Kann, D. et al. GCN22985 – OSN observation. *GCN Circulars* <https://gcn.gsfc.nasa.gov/gcn3/22985.gcn3> (2018).
- Martone, R. et al. GCN22976 – LCO Haleaka observation of GRB 180720B. *GCN Circulars* <https://gcn.gsfc.nasa.gov/gcn3/22976.gcn3> (2018).
- Zheng, W. et al. GCN23033 – KAIT observation of GRB 180720B. *GCN Circulars* <https://gcn.gsfc.nasa.gov/gcn3/23033.gcn3> (2018).

55. The Swift Burst Analyser – GRB 180720B [https://www.swift.ac.uk/burst\\_analyser/00848890/](https://www.swift.ac.uk/burst_analyser/00848890/) (2018).
56. Nousek, J. A. et al. Evidence for a canonical GRB afterglow light curve in the Swift/XRT data. *Astrophys. J.* **642**, 389–400 (2006).
57. Vurm, I. & Beloborodov, A. M. On the prospects of gamma-ray burst detection in the TeV band. *Astrophys. J.* **846**, 152 (2017).
58. Blandford, R. D. & McKee, C. F. Fluid dynamics of relativistic blast waves. *Phys. Fluids* **19**, 1130–1138 (1976).
59. Aharonian, F. A. *Very High Energy Cosmic Gamma Radiation: A Crucial Window on the Extreme Universe* (World Scientific Publishing, 2004).
60. Blumenthal, G. R. & Gould, R. J. Bremsstrahlung, synchrotron radiation, and Compton scattering of high-energy electrons traversing dilute gases. *Rev. Mod. Phys.* **42**, 237–270 (1970).
61. Kelner, S. R., Aharonian, F. A. & Khangulyan, D. On the jitter radiation. *Astrophys. J.* **774**, 61 (2013).
62. Santana, R., Barniol, D. & Kumar, P. Magnetic fields in relativistic collisionless shocks. *Astrophys. J.* **785**, 29 (2014).

**Acknowledgements** We acknowledge the support of the Namibian authorities and of the University of Namibia in facilitating the construction and operation of H.E.S.S. We also acknowledge support by the German Ministry for Education and Research (BMBF); the Max Planck Society; the German Research Foundation (DFG); the Helmholtz Association; the Alexander von Humboldt Foundation; the French Ministry of Higher Education, Research and Innovation; the Centre national de la recherche scientifique (CNRS/IN2P3 and CNRS/INSU); the Commissariat à l'énergie atomique et aux énergies alternatives (CEA); the UK Science and Technology Facilities Council (STFC); the Knut and Alice Wallenberg Foundation; the National Science Centre, Poland, through grant number 2016/22/M/ST9/00382; the South African Department of Science and Technology and National Research Foundation; the University of Namibia; the National Commission on Research, Science & Technology of Namibia (NCRST);

the Austrian Federal Ministry of Education, Science and Research; the Austrian Science Fund (FWF); the Australian Research Council (ARC); the Japan Society for the Promotion of Science; and the University of Amsterdam. We appreciate the work of the technical support staff in Berlin, Zeuthen, Heidelberg, Palaiseau, Paris, Saclay, Tübingen and in Namibia for the construction and operation of the equipment. This work benefited from services provided by the H.E.S.S. Virtual Organisation, supported by the national resource providers of the EGI Federation. The Fermi-LAT Collaboration acknowledges support for LAT development, operation and data analysis from NASA, the US Department of Energy (DOE), CEA/Irfu and IN2P3/CNRS (France), ASI and INFN (Italy), MEXT, KEK, JAXA (Japan), the K. A. Wallenberg Foundation, the Swedish Research Council and the National Space Board (Sweden). Science analysis support in the operations phase from INAF (Italy) and CNES (France) is also acknowledged. This work was performed in part under DOE contract DE-AC02-76SF00515.

**Author contributions** R.D.P., Q.P. and E.R.-V. analysed and interpreted the H.E.S.S. data and prepared the manuscript. E.B. analysed and interpreted the Fermi data and prepared the manuscript. C.H. implemented the response system for the GRBs follow-up of H.E.S.S. A.M.T., F.A. and D. Khangulyan helped to interpret the results and prepare the manuscript. The entire H.E.S.S. collaboration contributed to the publication with involvement at various stages, from the design, construction and operation of the instrument to the development and maintenance of all software for data handling, data reduction and data analysis. All authors reviewed, discussed and commented on the present results and the manuscript.

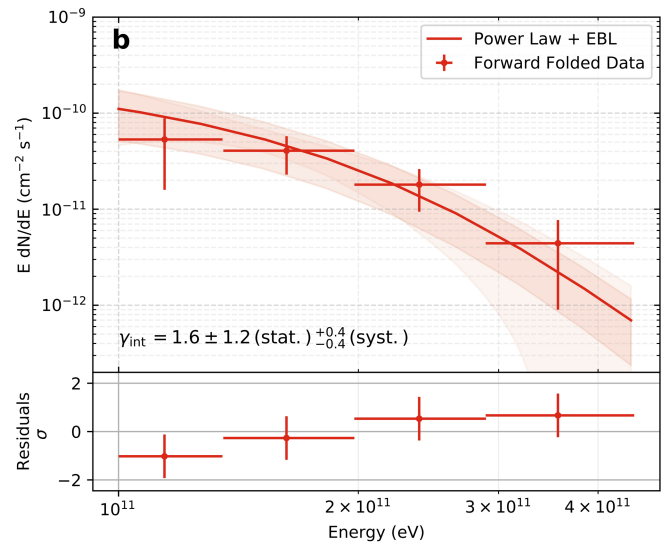
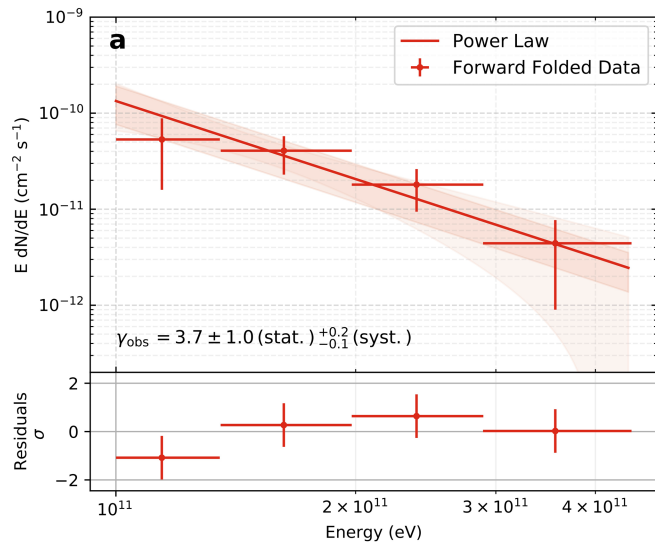
**Competing interests** The authors declare no competing interests.

**Additional information**

**Correspondence and requests for materials** should be addressed to E.R.-V.

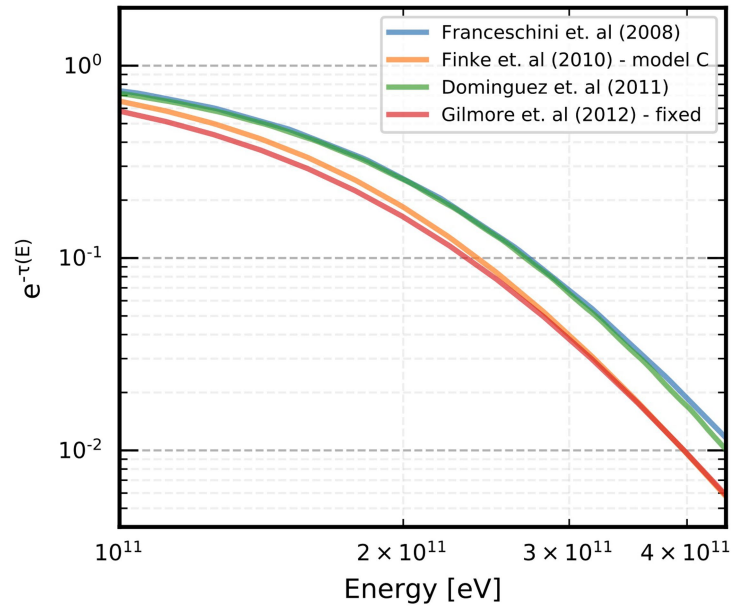
**Peer review information** *Nature* thanks Gus Sinnis and the other, anonymous, reviewer(s) for their contribution to the peer review of this work.

**Reprints and permissions information** is available at <http://www.nature.com/reprints>.

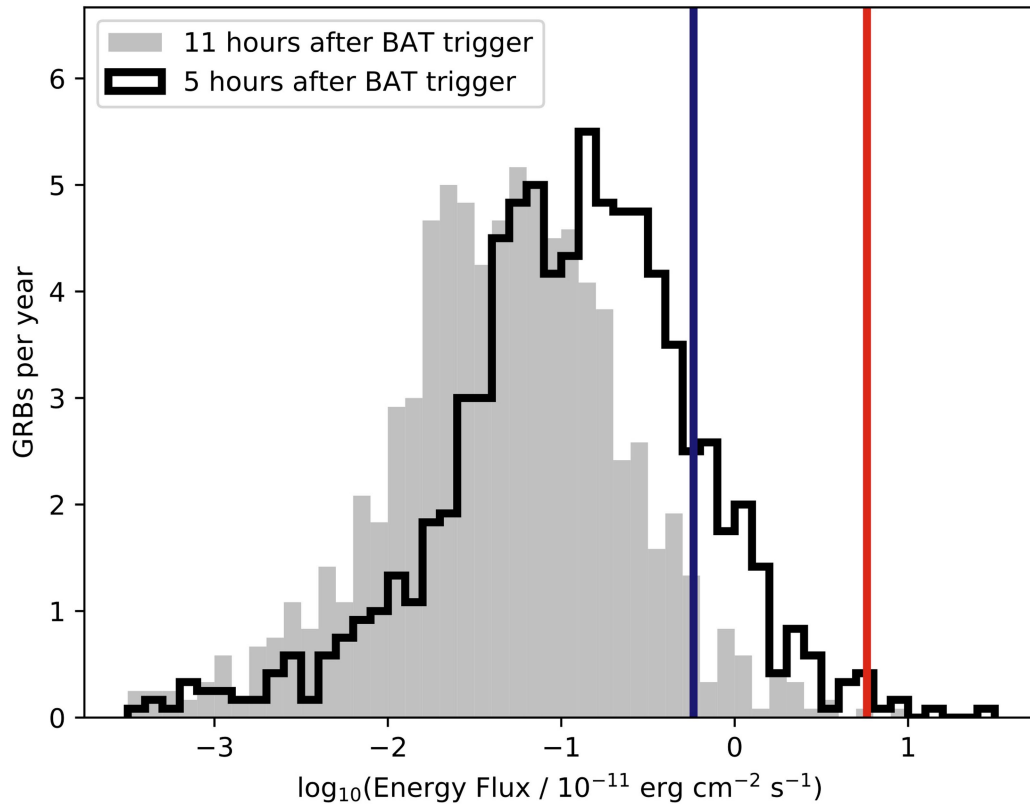


**Extended Data Fig. 1 | VHE spectral fit of GRB 180720B.** H.E.S.S. spectral fit to the measured emission in the energy range 100–440 GeV. **a.** Fit using a simple power-law model (with photon index  $\gamma_{\text{obs}}$ ). **b.** Fit with a power-law model (with photon index  $\gamma_{\text{int}}$ ) with EBL attenuation for a source at  $z = 0.653$  (ref. 13). In both

cases the residual data points with  $1\sigma$  uncertainties are obtained from the forward-folded method. The shaded areas show the statistical and systematic uncertainties in each fit ( $1\sigma$  confidence level). The bottom panels show the significance of the residuals between the fitted model and the data points.



**Extended Data Fig. 2 | EBL absorption coefficient.** Absorption coefficient  $e^{-\tau(E)}$  for a source emitting at a redshift of 0.653. The values are shown in the energy range of the detected emission of GRB 180720B (100–440 GeV) for the four EBL models considered<sup>13,39–41</sup>.



**Extended Data Fig. 3 | CTA detectability prospects.** Energy-flux distribution at 11 h and 5 h after the Swift-BAT trigger for all the GRBs observed by Swift-XRT per year. The blue vertical line shows the expected sensitivity of CTA, assuming

the detection of fluxes 10 times fainter than that of GRB 180720B. The energy flux of GRB 180720B is indicated by the red vertical line.

**Extended Data Table 1 | VHE spectral information from GRB 180720B**

Spectral model	$F_0$ [ $\times 10^{-10}$ cm $^{-2}$ s $^{-1}$ TeV $^{-1}$ ]	$\gamma$	$E_0$ [TeV]
$F_0 \times \frac{E}{E_0}^{-\gamma}$	$2.71 \pm 0.74^{+1.43}_{-1.16}$	$3.7 \pm 1.0^{+0.2}_{-0.1}$	0.154
$F_0 \times \frac{E}{E_0}^{-\gamma} \times e^{-\tau(z,E)}$	$7.52 \pm 2.03^{+4.53}_{-3.84}$	$1.6 \pm 1.2^{+0.4}_{-0.4}$	0.154
$F_0 \times \frac{E}{E_0}^{-2} \times e^{-\tau(z,E)}$	$16.12 \pm 4.37^{+10.59}_{-9.25}$	2.0 [Fixed]	0.105

Spectral parameters of the fits to the H.E.S.S. observed emission in the energy range 100–440 GeV. The intrinsic spectrum with  $\gamma=2.0$  (third row) is provided as a reference to the Fermi-LAT mean photon index detected in several other GRBs at high energies<sup>14</sup>. All reported uncertainties are statistical and systematic, in that order.